Biophysical Journal, Volume *112*

Supplemental Information

Line Tension Controls Liquid-Disordered + Liquid-Ordered Domain Size Transition in Lipid Bilayers

Rebecca D. Usery, Thais A. Enoki, Sanjula P. Wickramasinghe, Michael D. Weiner, Wen-Chyan Tsai, Mary B. Kim, Shu Wang, Thomas L. Torng, David G. Ackerman, Frederick A. Heberle, John Katsaras, and Gerald W. Feigenson

SUPPORTING MATERIAL

This supporting material contains detailed protocols and controls used in the experimental and theoretical procedure.

1. Line tension measurements

1. 1. Sample Preparation and cooling procedure

For ρ window measurements, samples contained 0.02 mol% C12:0 DiI; GUVs were made by electroformation with several modifications (1). The lipid films that formed after evaporation in vacuum were swelled at 45°C (when containing bSM, eSM or pSM) or 55°C (when containing DSPC) in 100 mM sucrose under a 5 Hz AC field for 2 h to form the GUVs. To measure ρ windows, the slides were cooled to room temperature (21°C) over 10 h and the vesicles harvested into 100 mM glucose solution in glass test tubes. Samples rested for ~ 1 h so that the sucrose-containing GUVs could settle through the less dense glucose solution. This procedure removes lipid debris, hence background signal, from the GUVs.

To measure line tension, samples contained 0.2 mol% C12:0 DiI, and GUVs were formed as above but were cooled in two different ways to form domains of a suitable size as described in the main text. For low ρ values, circular lipid domains with ~5 μm diameter were obtained by cooling GUVs from 50 to 23°C over ~ 3 h. For higher ρ values, very large round Ld + Lo domains formed over several hours, so the necessary smaller round domains were obtained by faster cooling. In detail, room temperature GUV samples were reheated briefly to 50°C, then 3-4 μl of the sample was deposited into the slide chamber maintained at either room temperature or cooled prior to sample deposition, depending on what was required to obtain ~5 μm diameter domains. Before imaging, GUVs were allowed to settle for 5 minutes on the microscope slide. Circular lipid domains with ~5-μm diameter were then studied at 23°C. The cooling procedure for each sample is summarized in Table S1, followed by a more detailed description of each protocol.

TABLE S1 Fast cooling techniques used in different four-lipid systems

Four-lipid systems	Composition	ρ values	Fast cooling setup
DSPC/DPhPC+DLPC/chol	0.5/0.23/0.27	0-0.2	Immediately visualized
		0.3-0.6	Heated up to 45^{o}C and quickly cooled to 23^{o}C
		0.8-1.0	Heated up to 45^{o}C and quickly cooled to 0^{o}C
DSPC/DOPC/POPC/chol	0.39/0.39/0.22	0-06	Cooled to room temperature over 10 hours, re-heated up to 50^{o}C and quickly cooled to room temperature
DSPC/DPhPC/POPC/chol	0.39/0.39/0.22	0-0.3	Cooled to room temperature over 10 hours, re-heated up to 50^{o}C and quickly cooled to room temperature
bSM/DOPC+POPC/chol	0.39/0.39/0.22	0.5-0.7	Cooled to room temperature over 10 hours and re-heated up to 50^{o}C and quickly cooled to 0^{o}C

		0.8-1.0	Cooled to room temperature over 10 hours, re-heated up to 50°C and quickly cooled to room temperature
eSM/DOPC+POPC/chol	0.39/0.39/0.22	0.1-0.2	Cooled over 3.5 hours + Heated up to 50°C and quickly cooled to room temperature
		0.3-1.0	Cooled to room temperature over 10 hours and re-heated up to 50°C and quickly cooled
pSM/DOPC+POPC/chol	0.39/0.39/0.22	0.0-0.05	Cooled over 3.5 hours
		0.1-1.0	Cooled to room temperature over 10 hours and re-heated up to 50°C and quickly cooled to room temperature
bSM/DOPC+POPC/chol + 4mol% WALP	0.39/0.39/0.22	0.1-0.25	Cooled over 3.5 hours
		0.35-1.0	Cooled to room temperature over 10 hours and re-heated up to 50°C and quickly cooled to room temperature

Cooled to room temperature over 10 hours and re-heated to 50 °C and quickly cooled to 0 °C:
Cooled from 45 °C to room temperature over 10 hours and harvested into 100 mM glucose and allowed to settle. The samples were heated back up to 50 °C and then 2-3µl were placed on a slide that had been cooled to 0 °C. The slide was allowed to return to room temperature before imaging.

Heated up to 50 °C and quickly cooled to room temperature:
Cooled from 45 °C to room temperature over 10 hours and harvested into 100 mM glucose and allowed to settle. The samples were heated back up to 50 °C and then 2-3µl were placed on a slide and imaged without any further heating or cooling processes.

Cooled over 3.5 hours:
Cooled from 45 °C to room temperature over 3.5 hours and harvested into 100 mM glucose and allowed to settle. 3-4µl were placed on a slide and imaged without any further heating or cooling processes.

1. 2. Sample Compositions

Sample compositions for each mixture were chosen based on which compositions produced small isolated domains. These compositions are displayed in Table S2.

TABLE S2. Sample composition used in the line tension measurements for six different lipid mixtures.

Mixture	High-Tm	Low-Tm	chol
PSM/DOPC/POPC/chol	0.39	0.39	0.22
eSM/DOPC/POPC/chol	0.39	0.39	0.22
bSM/DOPC/POPC/chol	0.39	0.39	0.22
DSPC/DOPC/POPC/chol	0.55	0.20	0.25
DSPC/DPhPC/POPC/chol	0.45	0.30	0.25
DSPC/DPhPC/DLPC/chol	0.50	0.23	0.27

1. 3. Optimizing Probe Concentration

The short exposure times required to capture domain fluctuations for line tension measurements necessitate intense illumination and/or high probe concentration. The potential for light-induced artifacts increases with both of these parameters (2). To limit artifacts during the optimization of probe concentration and data collection, we used a four-component mixture of fully saturated lipids: DSPC/DPhPC/DLPC/chol. DPhPC, when it is the only low-Tm lipid, gives rise to macroscopic phase separation, whereas DLPC as the sole low-Tm lipid yields nanodomains. Here, ρ = DPhPC/ DPhPC+DLPC. Initial tests of probe concentration were carried out at the ρ value where macroscopic phase separation first occurs for this four-component mixture. Increasing concentrations of probes, LR-DOPE and 12:0 DiI, were tested to achieve the best balance of GUV yield and contrast. 0.2 mol% C12:0 DiI proved to be ideal for line tension measurements. Higher probe concentrations tended to reduce yield while at the same time increasing the likelihood of light induced artifacts.

1. 4. Data Acquisition and Analysis

All microscopy measurements used an inverted Nikon Eclipse TI-E (Nikon Instruments), with a 60x 1.2 NA water immersion objective, and additional 1.5x intermediate magnifier for line tension measurements. Excitation of DiI was via a Spectra X Light Engine (Lumencor, Inc.) with a green LED (542/27). To narrow the wavelengths of excitation and emission, we used a filter cube with 545/25 excitation filter and 605/70 emission filter. Images were acquired using a Zyla 5.5 sCMOS camera (Andor Tehcnology Ltd) with 6.4μm pixels. With a total of 90x magnification for line tension, each pixel represented ~71nm. Data acquisition and control of illumination intensity were performed using the software NIS-Elements Basic Research (MVI, Inc).

For reliable line tension measurements, we looked at the top center of a GUV for approximately-circular domains greater than 5 μm in diameter but less than $1/5^{th}$ of the diameter of the entire GUV (3). For each domain, we acquired a 15 s time series: 10 ms exposure times with a 30 ms cycle time, yielding ~500 frames. A minimum of 10 such domains were imaged for each ρ value. It was a challenge to find domains that were both circular and of a useful size and at the top of the GUV. For all four-component mixtures, we can only start to measure line tension at a ρ value where phase separation is visible under the light microscope and for which circular domains can form. This was often at a ρ value just slightly higher than that at the first appearance of macroscopic domains. To find such domains, we searched the sample using fluorescence at a low 2% illumination intensity of the Spectra X. Once a useful domain was found, data were collected at 50% illumination intensity. During the acquisition, the Spectra X was

triggered by the camera so that the LED was only on during the 10 ms exposure time. During the 20 ms between frames, the LED was off. This reduced light exposure, minimizing light-induced artifacts.

Analysis of domain fluctuations was implemented using Matlab 2010a and followed the basic methodology of Baumgart et al (3). The software located domain boundaries throughout a time series using Matlab's Canny edge detection, taking the largest boundary to define the domain of interest (Fig. S1). A domain in a particular frame was only considered for analysis ("valid") when it was approximately circular and within 3% of the original domain area. The average Fourier transform of the valid boundaries was then used to calculate σ for each mode using Eq. 1 from the main text. The line tension of a domain was taken to be the average σ over modes $n = 2 – 5$. Averages were only considered valid if the time series had more than ~ 250 valid frames and produced relatively constant values of σ over modes $n = 2 – 5$.

We used only modes 2-5 for the analysis in part because they were shown by Baumgart et al. to effectively measure line tension, and also because we empirically found them to accurately measure line tensions in fluctuating domain simulations analogous to those described in Baumgart et al (3).

Evidence that this method works is shown in Fig. S1, where it is straightforward to see the differences in measured line tension for domains at low and high ρ. For bSM/DOPC/POPC/chol, macroscopic phase separation is first observed at $\rho \sim 0.50$ with a line tension value of 0.29 ± 0.04 pN (Fig. S1 *A*, *B*). At $\rho = 1.00$, the line tension is 1.3 ± 0.1 pN (Fig. S1 *C*, *D*). The greater fluctuation amplitudes visible in A and B are consistent with lower line tensions compared to C and D.

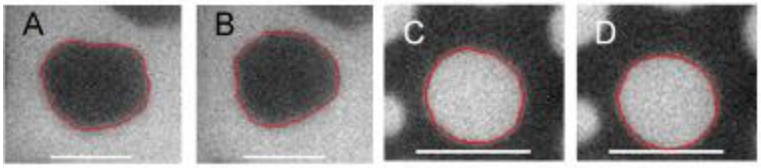

Fig. S1**.** Snapshots of domains over time, with detected boundaries outlined in red, show differences in line tension. A,B) Domain at $\rho = 0.5$ with an average line tension of 0.29 ± 0.04 pN. The time between A and B is ~ 0.75 s. C,D) Domain at $\rho = 1.00$ with line tension 1.31 ± 0.12 pN. The time between C and D is ~ 0.75 s. Scale bars are 5 μm.

1.5. Testing for light-induced effects on line tension

Since the dye concentration of 0.2% is rather high in order to achieve the required contrast, there is a possibility of light-induced artifacts. These can result in the break-up of domains, the fusion of domains, or a change in the amplitude and frequency of the fluctuations of the domains. Therefore, we always test for any light-induced artifacts by measuring the change in line tension over time. For each domain, the data were split into successive subsets of 100 frames (successive subsets of 3 s time intervals); the first subset containing data from time 0-3 s, the second subset containing data from time 3-6 s, etc. For a given domain, the line tension value for each subset was normalized to the line tension value in the first 100 frames. These data were then averaged together over all domains at each ρ value (Fig. S2). While there were some fluctuations in the normalized line tensions, most ρ values exhibited no illumination- or time-dependent trends. For DSPC/DOPC/POPC/chol, at $\rho = 0.2$, Fig. S2 shows a decrease in line tension by nearly 50% from the first subset to the second, for instance. This unreliable change is considered to be due to light induced artifacts, and this kind of data was then discarded. This composition was carefully remeasured to avoid light induced artifacts.

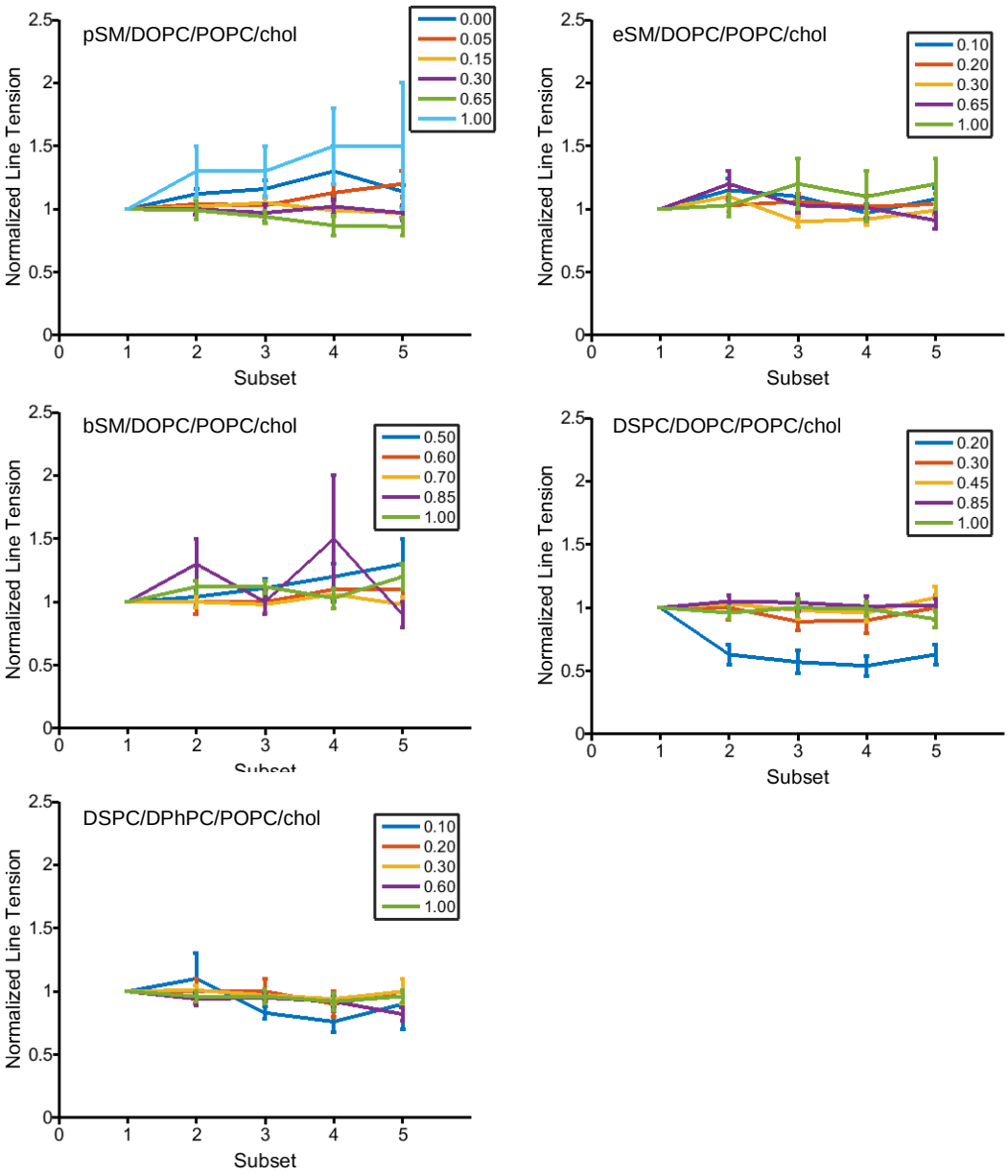

Fig. S2**.** Light-induced effects can be detected by measuring line tension over time. For these tests, an average line tension of each successive subset of 100 frames is normalized by the line tension in the first 100 frames. The legend indicates the system's ρ value.

The effect of such light-induced artifacts can be clearly seen in Fig. S3, where we show a single domain at this composition throughout its 15 s exposure. While the domain starts off round, by 15 s, its shape is very irregular. This data was discarded.

We note that for each of the 6 mixtures studied, the trend in line tension versus ρ was similar for each subset. This, together with the fact that most ρ values show no trend in line tension over time, allows us to conclude that light-induced effects were negligible.

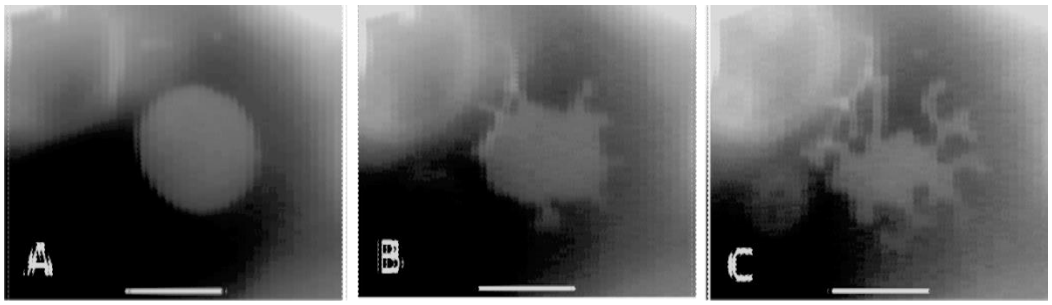

Fig. S3**.** Domain exhibiting light induced artifacts. Domain at ρ = 0.2 for DSPC/DOPC/POPC/chol, at A) t = 0 s, B) t = ~ 7.5 s, and C) t = ~15 s. This domain was not used for analysis, but shows how a round domain can become misshapen over time due to illumination. Scale bars are 5 μm.

1.6. Cooling Controls

To ensure that the measured line tension values did not differ based on the cooling method used — slow cooling over 3.5 hours or fast cooling over a few seconds — the pSM/DOPC/POPC/chol and eSM/DOPC/POPC/chol systems were imaged after making samples using both cooling protocols. Since different methods of cooling were required to obtain suitable domains for different ρ values, only a few ρ values for the pSM and eSM could be imaged using *both* methods of cooling. The line tension values observed show that the values of the line tension are within the standard error of each other and follow similar trends regardless of slower or faster cooling method (Fig. S4). The line tension values shown in the main text are the values obtained from domains using both cooling methods.

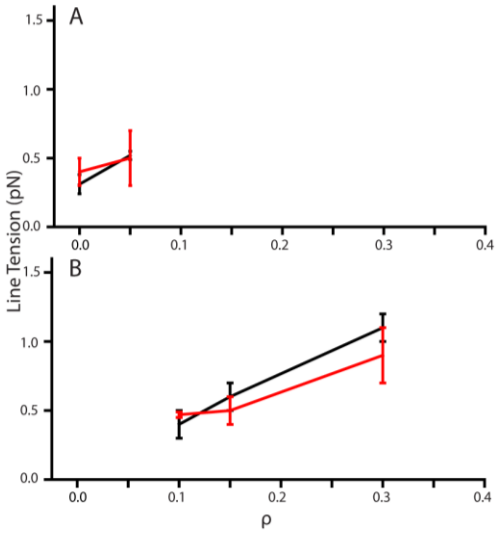

Fig. S4**.** Line tension measurements using faster (black) or slower cooling (red) are the same for A) pSM/DOPC/POPC/chol and B) eSM/DOPC/POPC/chol. Error bars: mean ± standard error.

1. 7. Size Dependence Controls

GUV and domain radii were recorded for all measurements. To ensure that the line tension measurement itself does not depend on the size of the domain or the size of the GUV it is on, we have compared normalized line tension to size, where line tensions were normalized to the average line tension for a given composition. In Fig. S5 *A* it can be seen that the normalized line tensions remain close to one,

meaning that line tension is independent of domain radius. Similarly, line tension is independent of GUV radius as shown in Fig. S5 *B*. The ratio of domain size to GUV size is another factor that could cause a distortion in measured line tension, but importantly, for the domains used in this study, the line tension measurement is independent of this ratio (Fig. S5 *C*).

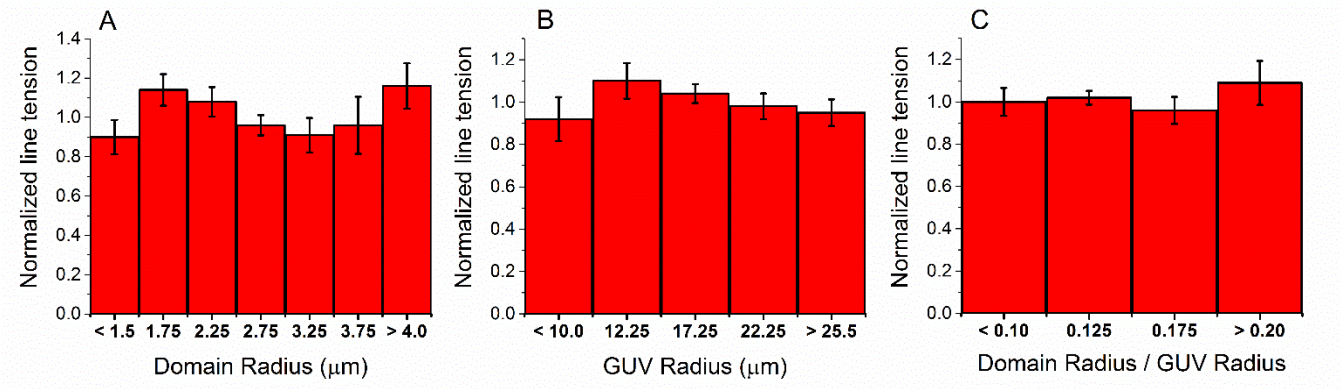

Fig. S5. DSPC/DPhPC/DLPC/chol line tension is independent of domain size and GUV size. At each ρ value each line tension measurement was normalized to the average of all measurements at that ρ value. Normalized line tension was compared to domain radius (A), to GUV radius (B) and to the ratio of the two (C). Bars reflect bins of approximately equal size.

2. Small Angle Neutron Scattering (SANS)

SANS $I(q)$ data were analyzed with a coarse-grained Monte Carlo method described in Heberle et al. (4). Briefly, vesicles were modeled as spherical shells of radius R_v and thickness t_{ac} corresponding to the hydrophobic thickness of the bilayer, with polydispersity assumed to follow a Schulz distribution (5). The shell volume was divided into one or more randomly placed, non-overlapping circular domains of radius R_d. Random points were generated within the shell volume in proportion to the neutron scattering length density (NSLD) contrast of the bilayer phases with the surrounding water using a rejection algorithm (*i.e.*, points were uniformly generated within the shell and tested for inclusion in a domain until both phases accumulated the desired number of points). The NSLD-weighted pair distance distribution $P(r)$ was calculated from the set of random points, and the procedure was repeated for 10^5 vesicles to obtain an ensemble average. The scattering intensity was then calculated as (6):

$$I(q) = 4\pi \int_0^\infty P(r) \frac{\sin qr}{qr} dr. \qquad \text{(S1)}$$

For best S/N in SANS measurements we used compositions where area fractions of Ld and Lo were nearly equal. Most trajectories for line tension measurements used the same compositions. Samples were prepared near the lowest-chol tieline of the Ld + Lo region where the compositions of the coexisting phases are well determined, which is a necessity for the bending energy and ESR experiments.

We explored a wider range of LUV size at a single ρ value to find any influence on measured nanodomain size. Fig. S6 shows domain sizes at ρ = 0 for DSPC/POPC/chol, obtained from extruded vesicles with nominal extrusion pore sizes ranging from 30 – 200 nm diameter (Fig. S6, open squares). Extrusion of neutral lipids using pore sizes ≥ 100 nm is known to generate a minor population of

paucilamellar vesicles (PLVs) that can be eliminated by adding a small fraction of charged lipid to the mixture (7). To test whether Bragg scattering from contaminating PLVs might affect the determination of domain size, samples were also prepared in which 5 mol% of each PC lipid was replaced with its PG counterpart (Fig. S6, diamonds). Within measurement uncertainty, domain size has a negligible dependence on vesicle size at $\rho = 0$: all measured domain radii fall in the range 5.0 – 6.8 nm. The presence of 5 mol% PG resulted in a ~5% decrease in domain size (Fig. S6).

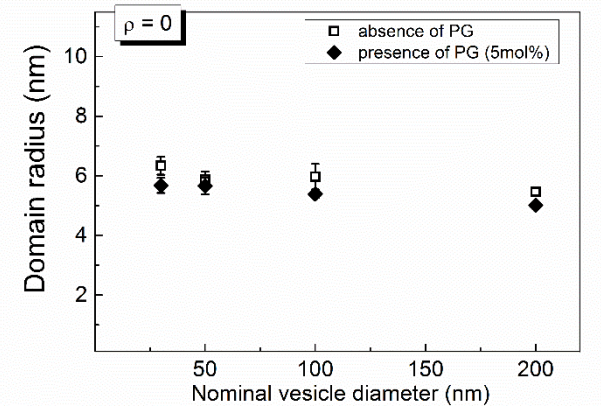

Fig. S6. SANS reveals that nanodomain size is independent of vesicle size. Domain radii obtained from Monte Carlo modeling of SANS data for LUVs composed of DSPC/POPC/chol = 39/39/22. At this $\rho = 0$ composition, the domain radius is independent of vesicle size and does not change significantly upon addition of 5 mol% charged lipid.

Discussion of Nanoscopic Phase Separation

As we discuss in detail in the main text, properties of Ld and Lo phases, such as bending energy, order parameter, rotational diffusion, and probe partitioning between phases gradually change on either side of the dramatic domain size transition and change rather little through the transition itself. In this sense the size transition does not have the hallmarks of a phase transition (8).

Previous experimental observations are consistent with Ld + Lo nanoscopic domains being phase separated mixtures. These mixtures were found to have all of the same phase coexistence regions as mixtures that show macroscopic domains. Indeed, the formation of Lo phase from Lβ phase occurs at $\chi chol \approx 0.16$ in all the mixtures we have studied, leading to similarities for different lipid mixtures in this region of the phase diagram (9–11). Of particular importance is the finding that the high-chol "upper" boundary of the Ld + Lβ coexistence region in a Gibbs Triangle phase diagram is a straight line in composition space in all the mixtures we have studied (9–11). This is readily explained if the region above Ld + Lβ is a three-phase coexistence triangle of Ld + Lβ + Lo, which has been directly verified for a macroscopic mixture by fluorescence microscopy observations (12). Because the Ld + Lβ upper boundary is linear in nanoscopic mixtures (10, 11), there is no critical point, consistent with an adjacent 3-phase region. In turn, this three-phase region must, according to the Phase Rule, be adjacent to a region with either four or two phases, inconsistent with this region being a one-phase microemulsion. Further, Goh et al. measured the areas of the modulated phase domains in GUVs and found the observed area fractions to follow the Lever-Arm Rule. This implies that the uniform surround must itself be a single phase, otherwise the Lever-Arm Rule would fail to describe the area fractions.

3. Molecular Dynamics (MD) simulations

Fig. S7 displays the full bilayer of a 20,000-lipid MD simulation at three ρ values: 0.5, 0.65, and 0.8. Each is displayed after phase separation, and the increasing size and connectivity of domains is visible as ρ increases. This increase in size and connectivity means a decrease in interface length between two phases, consistent with rising line tension. A 30 nm x 30 nm portion of the ρ = 0.65 plot (Fig. S7 *B*) which contains a single nanodomain is shown in the main body of this paper and was run for 3.6 μs. The other simulations represent the system after 1.2 μs. The additional time was found to not change phase morphology, implying 1.2 μs is sufficient for equilibration.

Any analysis on such a system depends on how we define a phase in a simulation. In order to prevent very small patches of one or a few lipids from being classified as domains, an adjustment was implemented: If a majority of a given lipid's nearest neighbors including itself were classified in the first round as being in a particular phase, the lipid was assigned to that phase in the second round. Our method is but one of several based on measuring local enrichment of high-Tm lipid (13, 14). A choice to compare neighboring phases twice is somewhat arbitrary but serves to remove clusters too small to be considered domains. Otherwise, the nonrandom clustering of lipids representing a small component of a phase can be mislabeled. A test of k-means clustering based on local composition revealed nearly identical classifications of lipids into phases. A further study of a large bilayer over a long time scale (> 10 μs), while computationally expensive, would provide further detail into the time-dependent properties of nanodomains, including their changing perimeters and whether individual domains form or disappear in a system already at equilibrium.

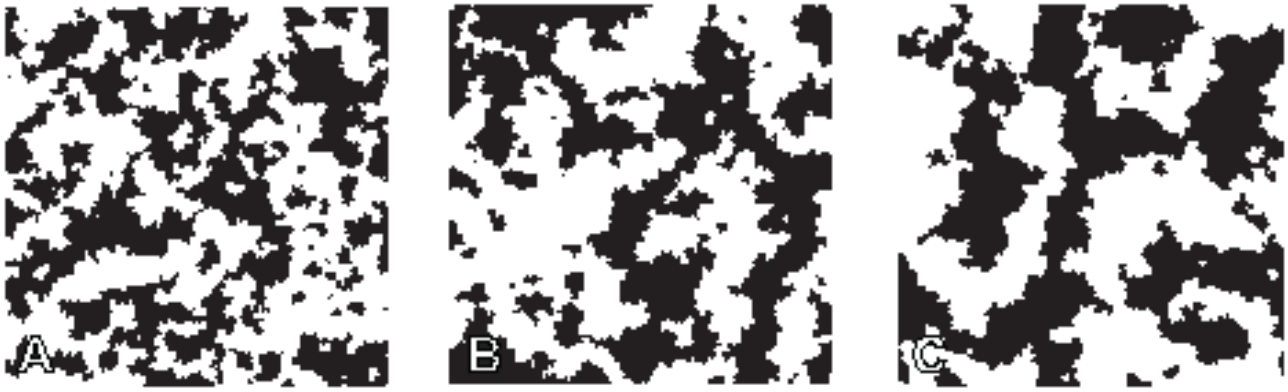

Fig. S7 Size and connectivity of domains increases as ρ increases. Lo is shown is black, and Ld is shown in white. Panels depict increasing ρ with (A) ρ = 0.5, (B) ρ = 0.65, and (C) ρ = 0.8. The visible decrease in interface length is consistent with rising line tension. Each simulation has a box size of approximately 74 nm x 74 nm.

Our Molecular Dynamics movie (included with this Supporting Material in a separate file, named MD_nanodomains.avi) demonstrates the dynamic shape and evolution of nanodomains. It shows the progression of a single 4-component system as it develops during phase separation and then continues rearranging. The time progression reveals the complex, non-circular morphology of a domain and its fluctuating nature. Lipids are colored by type (DUPC in blue, PUPC in cyan, DPPC in red, and cholesterol in yellow). Phases are not marked, but the formation of patches rich in DPPC and cholesterol (red and yellow) clearly shows the formation of Lo domains.

4. Bending Modulus measurement for DSPC/DOPC/POPC/chol

4.1. Sample composition

Bending modulus measurements were performed in DSPC/DOPC/POPC/chol using the lipid composition of Ld phase, DSPC/(DOPC+POPC)/chol = 0.10/0.80/0.10, or Lo phase, as described in Table S3. It should be noted that the right hand side of DSPC/DOPC/POPC/chol phase diagram changes with ρ. Therefore, the lipid composition used in Lo measurements smoothly change.

TABLE S3. Sample composition used in bending modulus measurements, showing only Lo phase of DSPC/DOPC/POPC/chol.

ρ	DSPC	(DOPC+POPC)	chol
0	0.58	0.17	0.25
0.2	0.62	0.11	0.26
0.35	0.64	0.09	0.27
0.6	0.67	0.06	0.28
0.8	0.67	0.05	0.28
1	0.68	0.04	0.28

4.2. Analysis Methods and Validation

Fig. S8 shows an example of edge detection and the bilayer fluctuations. For these experiments, a 4% difference in osmolality between inner and outer solutions was created, yielding slightly flaccid vesicles suitable for the measurement. Given the density difference of the solutions, vesicles with radii > 20 μm were excluded to avoid significant distortion due to gravity (15). Vesicles of radii < 10μm have too few pixels defining the contour, leading to poor statistics, and thus were also excluded. Only vesicles exhibiting visible fluctuations and free of defects like tethers, buds, or attachments were imaged. Vesicles contained 0.02 mol% C12 DiI to enable line scans of fluorescent dye intensity to identify and exclude multilayered vesicles.

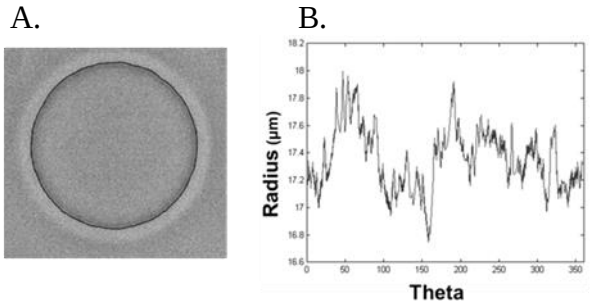

Fig. S8. Fluctuation Spectroscopy Edge Detection. (A) Fluctuations were observed with phase contrast images of the vesicle equator. Contour as defined by Canny edge detection is superimposed in black. (B) Fluctuation spectrum from the contour shown, where theta refers to points on the quasi-circular contour.

Our method for measuring bending moduli closely followed the methods of Gracià et al. (16). Our determination of the range of useful mode numbers hinged on the following considerations: Tension predominates for low modes, and high modes become indistinguishable from noise. Thus an intermediate range of modes, numbers 10 to 20, provides a reliable measure of the bending modulus (16). Measurements which did not result in a plateau of these modes were considered unreliable and excluded from the composition average.

To determine appropriate exposure times, we analyzed the relaxation time of various modes according to: $(4\,\eta\,R^3)/(\kappa_c m^3)$, where η is viscosity, R is radius, κ is the bending modulus, and m is the mode number (17). We determined that 1 ms is an adequate exposure time for the range of bending moduli in our experiments. The Spectra X white light source used for these experiments was triggered by the camera and remained off for 29 ms of the 30 ms cycle time used. Each dataset per vesicle measured included 1600 exposures. Achieving sufficient contrast requires moderately intense light, so we investigated the possibility of light-induced artifacts. For each measurement, datasets were divided into 200-frame subsets. No trends in these subsets were observed (data not shown). We confirmed that our procedure yields values similar to the bending moduli obtained by others (16, 18).

5. Single-Dye Fluorescence Trajectories

5.1. Phase Diagram and Sample Trajectories

Fig. S9 shows the phase diagram for bSM/POPC/chol (ρ = 0) and bSM/DOPC/chol (ρ = 1) and the lipid composition of 61 samples prepared along a thermodynamic tieline (two-phase region). These phase diagrams in Fig. S9 are similar to the ones reported in Ref. (11), but here we updated the boundaries somewhat with new measurements. For the intermediate trajectories obtained for ρ = 0.4 and ρ = 0.75, we interpolated the phase boundaries linearly with ρ. The Kp determination depends on the Lo and Ld phase fractions. The inserted axis in the phase diagram displays the fraction of Lo phase, χ_{Lo}, which represents the independent variable of Eq. (S3) below. The arrows labeled 1 and 2 point to phase boundaries of the coexistence region and represent pure Ld and Lo phases, respectively.

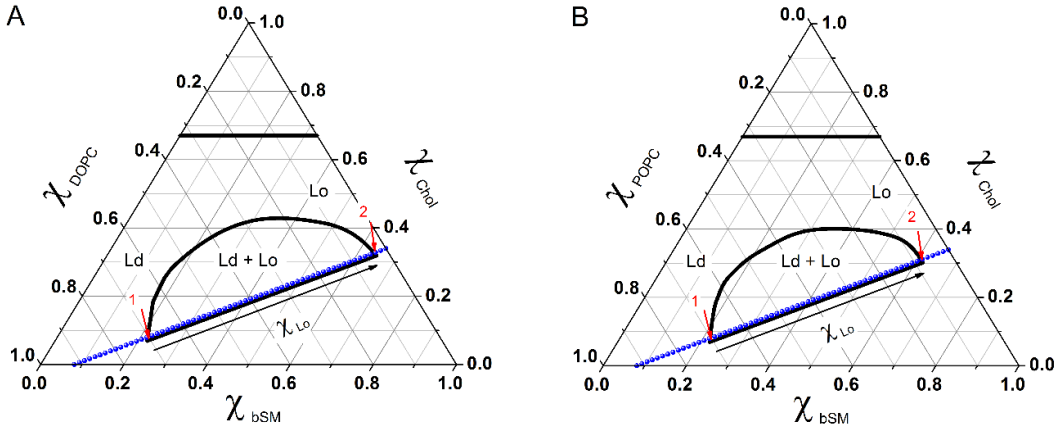

Fig. S9. Phase diagram of (A) bSM/POPC/chol (ρ = 0) and (B) bSM/DOPC/chol (ρ = 1). Sample trajectories were prepared with the lipid compositions shown in the phase diagram (blue). The inserted axis in the phase diagram displays the fraction of Lo phase, χ_{Lo}, and the arrows labeled 1 and 2 point to the phase boundaries of the coexistence region.

5.2. Quenching Correction

For the fluorescence trajectories, dyes were used at a concentration that does not exhibit large self-quenching effects, as displayed in Fig. S10. This study of fluorescence self-quenching is also important for quenching corrections if necessary.

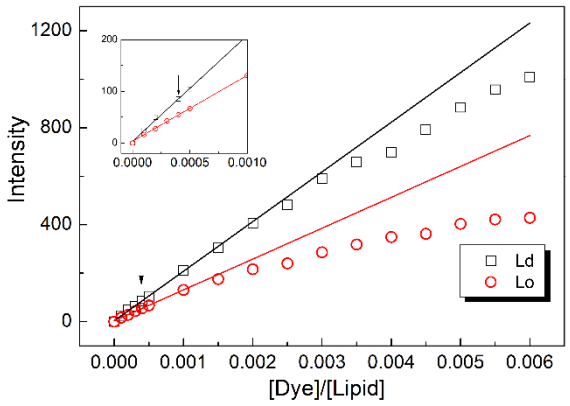

Fig. S10. Fluorescence self-quenching with increasing dye concentration. The self-quenching curve of Bodipy-PC for bSM/DOPC/chol in Ld and Lo phases (composition labeled 1 and 2, respectively, Fig. S9 *A*) is shown. The inset shows the linearity of Intensity and [dye]/[lipid] at low [dye]/[lipid] ratios. The small arrow displayed in the graph points to the [dye]/[lipid]=1/2500 ratio used in the fluorescence experiments.

5.3. Partition Coefficient Analysis

Fig. S11 shows the fluorescence trajectory for bSM/POPC/chol ($\rho = 0$) (also displayed in the inset of Fig. 5). The data were fitted using Eq. S3 below, where χ_{Lo} is the fraction of Lo phase, as shown in Fig. S9.

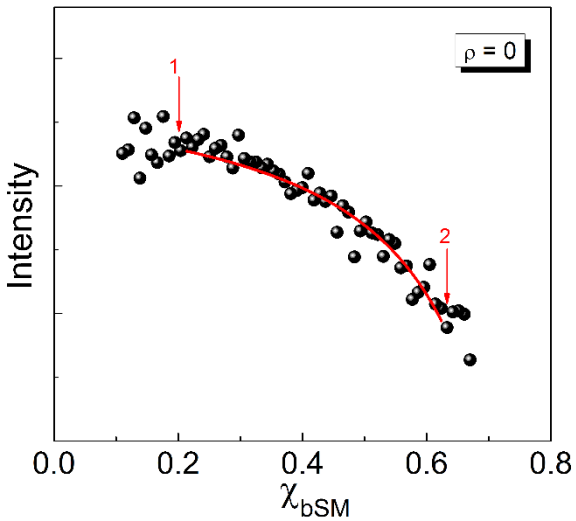

Fig. S11. Fluorescence emission of Bodipy-PC in bSM/POPC/chol. The lipid composition of each sample is displayed in the tieline of Fig. S9. The single dye fluorescence (corrected for quenching effects) was analyzed according to Eq. (S2).

The single dye fluorescence along a tieline is given by

$$F = \frac{F_{Ld}\, Kp\,(1-\chi_{Lo})+F_{Lo}\,\chi_{Lo}}{Kp\,(1-\chi_{Lo})+\,\chi_{Lo}} \quad \text{(S2)}$$

where F_{Ld} and F_{Lo} are the fluorescence signals from pure Ld and Lo phases, (i.e. the fluorescence at the lipid compositions represented by 1 and 2 in Fig. S11). The partition coefficient is defined by

$$Kp \equiv \frac{n_{Ld}/\chi Ld}{n_{Lo}/\chi Lo} \quad \text{(S3)}$$

such that Kp > 1 indicates partitioning that favors the Ld phase, and n_{Ld} and n_{Lo} indicate the fraction of dye in Ld and Lo phase, respectively. The error bars displayed in the Figure 5A were calculated by the goodness of fit of Eq. (S2).

6. Probe Partition Coefficient Determination for GUVs

We used line scans in GUV snapshots to measure the fluorescence intensity ratio between Ld and Lo phases. ImageJ was used to analyze snapshots and record intensity profiles. The intensity ratio between Ld and Lo phases was calculated using the area under the peak in the intensity profiles after subtracting the background intensity. Here, we performed 10 line scans for each phase in a single GUV, and we repeated this procedure for 5-10 different GUVs.

Bodipy-PC is intrinsically brighter in Ld phase compared to Lo phase. It is well known that fluorescent dyes can have different quantum yield (intensities) in different environments (19). Here, we have corrected the intensity ratio between Ld and Lo phases, obtained from the line scans, for the intrinsic fluorescence of the dye in each single phase.

In addition, the partition coefficient obtained by fluorescence trajectories is related to the total fluorescence that comes from Lo and Ld phases. This quantification differs from a single measurement of fluorescent intensity in Ld and Lo phases, as obtained from the line scans. Therefore, in order to compare the partition coefficient obtained using these two different techniques of fluorescence trajectories and fluorescence microscopy, we considered in our calculations that the Lo phase occupies 30% less area than the Ld phase (20, 21), in order to account for the total intensities from Ld and Lo, observed in the GUVs studies.

Fig. S12 displays an example of the partition coefficient measurement in GUVs. The snapshot in Fig. S12 *A* represents a typical line scan of Ld and Lo phases. Fig. S12 *B* displays the 10 different line scans for each phase used in the calculations of the partition coefficient. The error bars displayed in Figure 5A for Kp measurements on GUVs correspond to standard error of 5-10 GUVs, with 10 line scans for each phase.

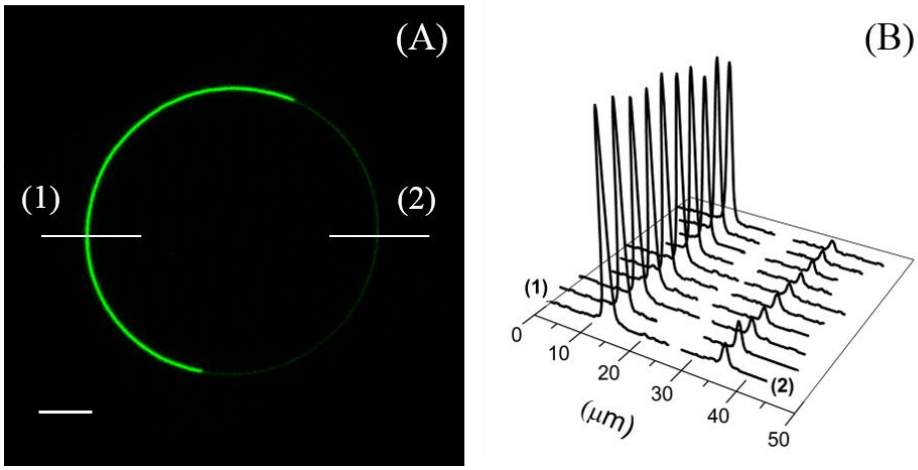

Fig. S12. Intensity profile measurements on GUVs. GUV lipid composition bSM/(DOPC+POPC)/chol = 0.4/0.4/0.2, dye/lipid = 1/2500. (A) Snapshot of a GUV, which exhibits Ld (brighter) and Lo phase separation. Lines labeled by the numbers (1) and (2) are line scans obtained in Ld and Lo phase, respectively. (B) Examples of 10 different line scans measured along Ld (brighter) and Lo phases. Scale bar: 5 μm.

7. Electron spin resonance (ESR)

The ESR spectrum of 111 samples measured along ρ for DSPC/DOPC/POPC/chol were analyzed according to equation:

$$S(\rho) = (1 - n_{Lo}) * Ld(\rho) + n_{Lo} * Lo(\rho) \qquad \text{(S4)}$$

where *Ld(ρ)* and *Lo(ρ)* correspond to the characteristic spectrum of Ld and Lo phase for a certain value of ρ, and $n_{Ld} = (1 - n_{Lo})$ and n_{Lo} represent the fractions of paramagnetic probe in Ld and Lo phase, respectively. Additionally, the characteristic spectra of Ld and Lo phases can be written as a linear combination of the spectra measured in ρ = 0 (DSPC/POPC/chol) and ρ = 1 (DSPC/DOPC/chol), according to Eqs. S5 and S6.

$$Ld(\rho) = (1 - \rho) * Ld(0) + \rho * Ld(1) \qquad \text{(S5)}$$

$$Lo(\rho) = (1 - \rho) * Lo(0) + \rho * Lo(1) \qquad \text{(S6)}$$

The partition coefficient is defined according to Eq. S3, except in this case n_{Ld} and n_{Lo} refer to the fraction of 16PC spin label. As mentioned above, χLd and χLo are the fractions of Ld and Lo phase.

Fig. S13 shows the spectra of (A) Ld phase and (B) Lo phase, for ρ = 0, 0.3 and 1. These spectra represent the phase morphologies of nano domains, modulated phases and macro domains, respectively. We observed small changes in the ESR spectra along ρ reflecting small changes in the order parameter and the rotational diffusion as shown in Table 1.

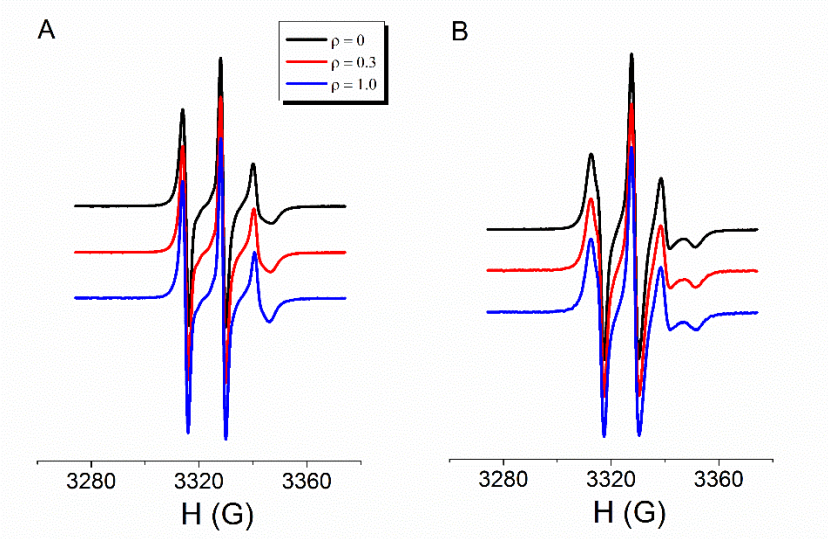

Fig. S13 ESR Spectra change little along ρ for both Ld and Lo. (A) Ld phase spectra. (B) Lo phase spectra. ρ = 0 is shown in black, 0.3 in red and 1in blue. Spectra are shifted for clarity.

8. Dipole-Dipole Repulsion Model

In order to explore the implications of dipole repulsion for domain size, we model the total energy of a phase-separated bilayer as a sum of a phase boundary energy from line tension that scales with domain perimeter and an electrostatic potential energy arising from permanent lipid dipoles.

An initial question for these studies is whether dipoles in one leaflet would have their fields largely cancelled by the opposing dipoles in the other leaflet. This does occur for the methyl dipoles that give rise to long-range repulsion in lipid monolayers (22). The dipoles of interest in this study would be farther apart, as shown in Fig. S14, suggesting that the oppositely oriented dipoles would not cancel. This was conclusively shown in the calculations described below and in the main text, wherein two leaflets of oppositely oriented dipoles produce a net repulsive electrostatic interaction when their magnitude and separation distance is comparable to carbonyl groups in a lipid bilayer.

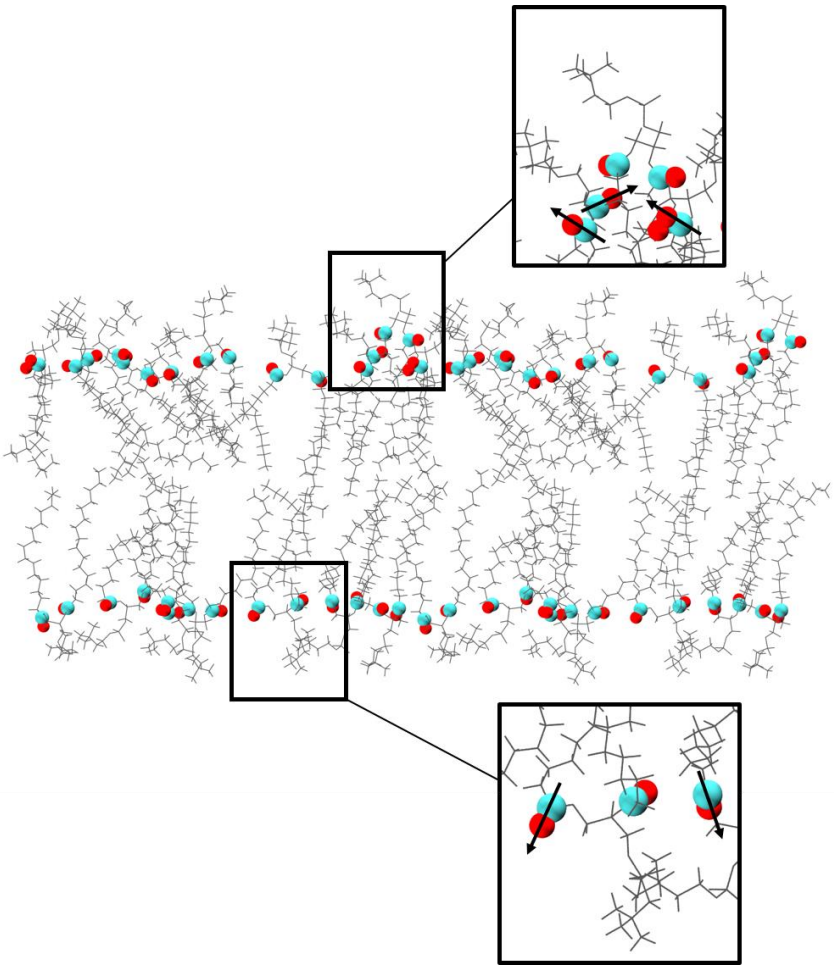

Fig. S14. The direction and location of carbonyl dipoles in a bilayer. Carbonyl groups at the top of each acyl chain are presented as spheres (cyan for carbon and red for oxygen), while the rest of the phospholipid is presented as gray lines. Dipoles drawn pointing from the positive carbon toward the negative oxygen along the bond reveal that the net dipole moment of each leaflet is normal to the bilayer and pointed outward toward the water (inset) and that there is individual variation in the dipole alignment. Phospholipids are displayed in each leaflet as a representation of a system obtained from Molecular Dynamics simulations of a DPPC bilayer.

For the calculations, we needed to determine the energetically favorable domain size for a set of lipid parameters. We therefore chose a fixed total domain area α and varied the number of domains N_D into which that area was divided; assuming circular domains, the domain radius is given by $R_D = \sqrt{\alpha/(\pi N_D)}$. The energetically favorable domain size R_D^* is defined as that which results in the lowest energy for a given set of parameters defined below.

The energetic contribution from the line tension σ is given by $2\pi R_D N_D \sigma$. To determine the electrostatic contribution, we first considered the electrostatic potential energy for an arbitrary arrangement of discrete dipoles in a membrane:

$$V = \frac{1}{4\pi\varepsilon\varepsilon_0}\sum_{i=1}^{N_L-1}\sum_{j=i+1}^{N_L}\left[\frac{\overrightarrow{\boldsymbol{p_i}}\cdot\overrightarrow{\boldsymbol{p_j}}}{\left\|\overrightarrow{\boldsymbol{r_{ij}}}\right\|^3} - \frac{3\left(\overrightarrow{\boldsymbol{p_i}}\cdot\overrightarrow{\boldsymbol{r_{ij}}}\right)\left(\overrightarrow{\boldsymbol{p_j}}\cdot\overrightarrow{\boldsymbol{r_{ij}}}\right)}{\left\|\overrightarrow{\boldsymbol{r_{ij}}}\right\|^5}\right], \qquad (S7)$$

where ε_0 is the permittivity of free space, ε is the dielectric constant (here, the dielectric constant of the bilayer region near the dipoles), N_L is the number of dipoles (here, the number of lipids possessing a permanent dipole), $\overrightarrow{\boldsymbol{p_i}}$ are the dipole moment vectors, $\overrightarrow{\boldsymbol{r_{ij}}}$ are the vectors connecting a pair of dipoles, and $\left\|\overrightarrow{\boldsymbol{r_{ij}}}\right\|$ are the distances between these dipole pairs. For lipids distributed identically in the two bilayer leaflets and dipoles aligned with the bilayer normal, the total electrostatic potential energy of the bilayer is a sum of intra- and interleaflet contributions, i.e. $V_{total} = 2V_{intra} + V_{inter}$, with

$$V_{intra} = \frac{1}{4\pi\varepsilon\varepsilon_0}\sum_{i=1}^{N_L^{top}-1}\sum_{j=i+1}^{N_L^{top}}\left(\frac{(p_i p_j)^2}{\left\|\overrightarrow{\boldsymbol{r_{ij}}}\right\|^3}\right), \qquad (S8)$$

$$V_{inter} = \frac{1}{4\pi\varepsilon\varepsilon_0}\sum_{i=1}^{N_L^{top}}\sum_{j=1}^{N_L^{bot}}\left(\frac{3(hp_i p_j)^2}{\left\|\overrightarrow{\boldsymbol{r_{ij}}}\right\|^5} - \frac{(p_i p_j)^2}{\left\|\overrightarrow{\boldsymbol{r_{ij}}}\right\|^3}\right). \qquad (S9)$$

Here, N_L^{top} and N_L^{bot} are the number of lipids in the top and bottom leaflets (with one net permanent dipole assigned to each), h is the bilayer thickness, and p_i are the dipole magnitudes. To simplify the calculations, we assumed that the domain and its surround differed only in the magnitudes of their dipoles, and that the main effect of electrostatics on domain size was due to the difference in dipole magnitudes between domain and surround, rather than their absolute values. With these assumptions, we set $p_{sur} = 0$, and replaced p_{dom} with $\Delta\phi\varepsilon\varepsilon_0 A_L$, where $\Delta\phi$ is the electrostatic potential difference between the domain and surround and A_L is the area per lipid in the domain. Our final simplification was to assume that domains are far enough apart that inter-domain energies are negligible. The total intra- and interleaflet contributions can then be rewritten as:

$$V_{intra} = \frac{N_D}{4\pi\varepsilon\varepsilon_0}\sum_{i=1}^{N_L^{top}-1}\sum_{j=i+1}^{N_L^{top}}\left(\frac{(\Delta\phi\varepsilon\varepsilon_0 A_L)^2}{\left\|\overrightarrow{\boldsymbol{r_{ij}}}\right\|^3}\right), \qquad (S10)$$

$$V_{inter} = \frac{N_D}{4\pi\varepsilon\varepsilon_0}\sum_{i=1}^{N_L^{top}}\sum_{j=1}^{N_L^{bot}}\left(\frac{3(h\Delta\phi\varepsilon\varepsilon_0 A_L)^2}{\left\|\overrightarrow{\boldsymbol{r_{ij}}}\right\|^5} - \frac{(\Delta\phi\varepsilon\varepsilon_0 A_L)^2}{\left\|\overrightarrow{\boldsymbol{r_{ij}}}\right\|^3}\right), \qquad (S11)$$

where N_L^{top} and N_L^{bot} now refer to lipid dipoles within a single domain.

In the continuum limit, as described in the main text, the discrete summations are replaced by integrals:

$$V_{intra} = N_D \frac{1}{2} \frac{{N_L}^2}{4\pi\varepsilon\varepsilon_0} \int_a^{2R_D} \frac{(\Delta\phi\varepsilon\varepsilon_0 A_L)^2}{r^3} P(r, R_D) dr, \qquad (S12)$$

$$V_{inter} = N_D \frac{{N_L}^2}{4\pi\varepsilon\varepsilon_0} \int_0^{2R_D} \left[\frac{3(h\Delta\phi\varepsilon\varepsilon_0 A_L)^2}{(h^2 + r^2)^{5/2}} - \frac{(\Delta\phi\varepsilon\varepsilon_0 A_L)^2}{(h^2 + r^2)^{3/2}} \right] P(r, R_D) dr, \qquad (S13)$$

where $a = 2\sqrt{A_L/\pi}$ (the lower limit of the V_{intra} integral) is the distance of closest approach between two dipoles, N_L is the total number of lipid dipoles in one domain leaflet, and $P(r, R_D)$ is the distribution of dipole separation distances derived as follows. Considering a vector $\boldsymbol{v} = (r\sin\theta, r\cos\theta)$ contained within the domain, the probability density for all vectors of magnitude r is proportional both to r, and to the overlap area A of two disks of radius R_D whose centers are separated by a distance r, as shown by the shaded region in Fig. S15*a*. This area is given by:

$$A(r, R_D) = 4 \int_{r/2}^{R_D} dx \sqrt{R_D - x^2} = 2{R_D}^2 \tan^{-1}\left[\frac{R_D}{r} \sqrt{4 - \left(\frac{r}{R_D}\right)^2} \right] - \frac{rR_D}{2} \sqrt{4 - \left(\frac{r}{R_D}\right)^2}. \qquad (S14)$$

The normalized probability distribution is then given by:

$$P(r, R_D) = \frac{rA(r, R_D)}{\int_0^{2R_D} rA(r, R_D) dr} = \frac{r}{\pi {R_D}^3} \left\{ 4R_D \tan^{-1}\left[\frac{R_D}{r} \sqrt{4 - (r/R_D)^2} \right] - r\sqrt{4 - (r/R_D)^2} \right\}. \qquad (S15)$$

Fig. S15*b* plots Eq. S15 for R_D = 10 (solid blue line), as well as a histogram of pair-distances obtained by generating 10^4 random points within a disk of radius 10, demonstrating the validity of the analytical solution.

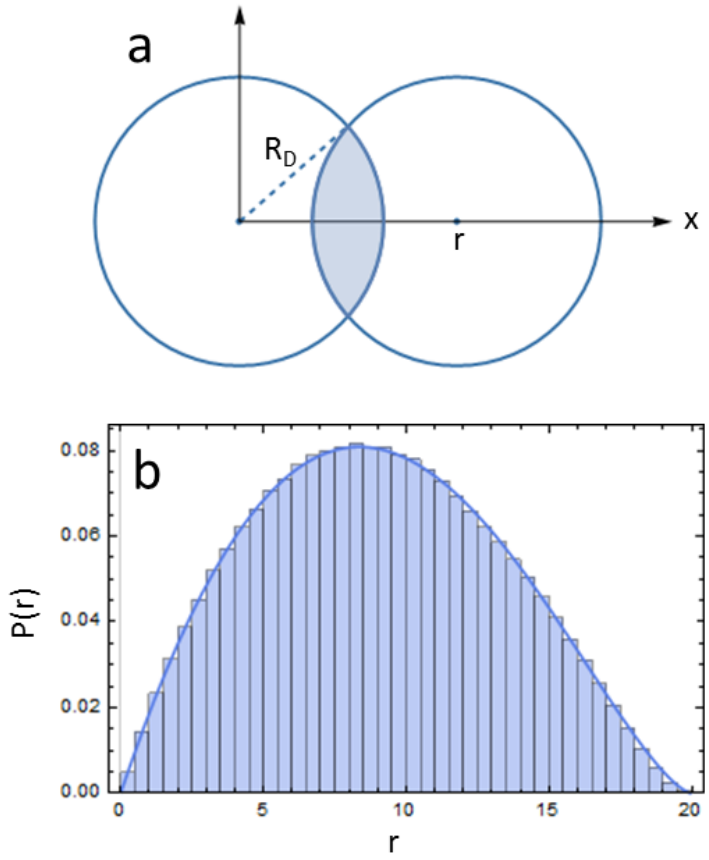

Fig. S15. Analytical solution for the pair-distance distribution function of a disk. *a*, geometric interpretation of the density of vectors of magnitude r contained with a disk of radius R_D as an overlap area. *b*, Eq. S15 plotted for R_D = 10 (solid blue line) and a corresponding pair-distance histogram generated from random points as described in the text, demonstrating the validity of the analytical solution.

For the calculations presented in the main text, we chose parameters reasonable for model bilayer membranes: $\varepsilon = 8$, $A_L = 60$ Å^2, $h = 3$ nm, $\Delta\phi$= 0.1 or 0.2 V, and total domain area $\alpha = \pi\ 30^2$ μm^2, corresponding to a single domain with a 30 μm radius.

In addition to the dipole continuum model discussed in the main text, we also calculated equilibrium domain sizes using three related models:

1. Modeling more explicitly the SANS experiment, we calculated the energetically favorable domain size for circular domains within a 60 nm diameter spherical vesicle; domain and surrounding membrane were assigned continuous dipole distributions with dipole potentials of 1 V and 0.9 V respectively, giving a dipole difference $\Delta\phi = 0.1$ V, or $\Delta\phi = 0.2$ V as in the isolated domain continuum model of the main text. Monte Carlo sampling was then used to calculate the distance distributions within domain and surround and between domain and surround, from which the electrostatic potential was calculated. The total domain area was fixed at 40% of the vesicle surface for this and the remaining two models.

2. We calculated the energetically favorable domain size as in the main text, but using discrete dipoles rather than the continuum limit. Within the circular domain, dipoles were assigned a magnitude of $0.1\ V * (\varepsilon\varepsilon_0 A_L) = 1.0617$ Debye and distributed approximately uniformly using a Matlab script (23).

3. We replaced the above discrete dipoles with discrete positive and negative charges calculated from the aforementioned dipole magnitude, assuming a dipole length of 1.23 Å (a typical carbonyl bond length), yielding charge magnitudes of ~ 0.18 e^-. In each model, h, ε and A_L are the same as in the main text.

For all models, we fixed the total domain area and chose reasonable values for membrane electrostatic properties, varying only the number of domains. For the three models discussed above, computational limitations prevent accessing arbitrarily large domain sizes: for these models, we chose a bilayer surface area corresponding to a ~ 60 nm diameter vesicle that resulted in a single "macrodomain" limit of R_d ~ 40 nm (to facilitate comparison, we also applied the continuum model to this case).

All four models reveal a sharp transition from many smaller domains, to a single large domain that is limited only by the vesicle size, with increasing line tension. Moreover, for all four models this transition occurs at similar values of line tension. Slight differences between the models are also evident. For example, treating the systems continuously versus discretely results in small differences in the line tension value required to induce the domain size transition. The stepwise nature of the vesicle continuum model arises due to computational limitations in fully sampling all possible numbers of domains, and the steps in the discrete models arises from the constraint that the number of dipoles per domain must be an integer value. Nevertheless, the four models are in good agreement over the range of accessible parameter space. Especially importantly, each model predicts an abrupt domain size transition at intermediate line tensions, indicating that continuum models can faithfully reproduce the discretization of real membranes. Despite differences in the models, we find that the vesicle model produces results which agree with the simplified continuum model, thus supporting the analysis methodologies and assumptions of the main text (namely that the main electrostatic effect is due to differences in electrostatic potential between domain and surround such that the surround can be ignored in favor of more simple analyses involving a flat, isolated domain). These models also show that the nature of the two competing interactions of line tension and electrostatics favor an abrupt transition in domain size and are not sensitive to the exact values used in the models until they take on unphysically large or small values (Figs. S16 and S17 described further below).

8.2 Model Sensitivity

As mentioned in the main text, the precise line tension value where the domain size transition occurs is sensitive to the choice of model parameters. However, the finding of an abrupt transition is robust, occurring for a wide range of parameter values as described below.

We investigated the influence of the parameters displayed in Table S4 by independently varying each parameter in the calculations. Fig. S16 plots the equilibrium domain radius as a function of the line tension for different values of dielectric constant, $\boldsymbol{\varepsilon}$, while holding other parameter values ($\boldsymbol{A_L}$, $\boldsymbol{h}$ and $\Delta\boldsymbol{\phi}$) constant as displayed in Table S4.

Table S4. Parameters used in the dipole-dipole repulsion simulations.

Parameter	Canonical value	Description
$\boldsymbol{\varepsilon}$	8	Dielectric constant
$\boldsymbol{\Delta\phi}$	0.2 V	Dipole potential difference between domain and surrounding phases
$\boldsymbol{h}$	3.0 nm	Separation distance between dipole planes in opposing leaflets
$\boldsymbol{A_L}$	60 Å^2	Area per dipole

For convenience, we label the line tension value where the domain size transition occurs as λ*. We found that, upon increasing the dielectric constant, the line tension value required to form macroscopic domains decreased, as displayed in Fig. S16. This result is physically intuitive, since an increase in the dielectric constant should decrease the influence of electrostatics.

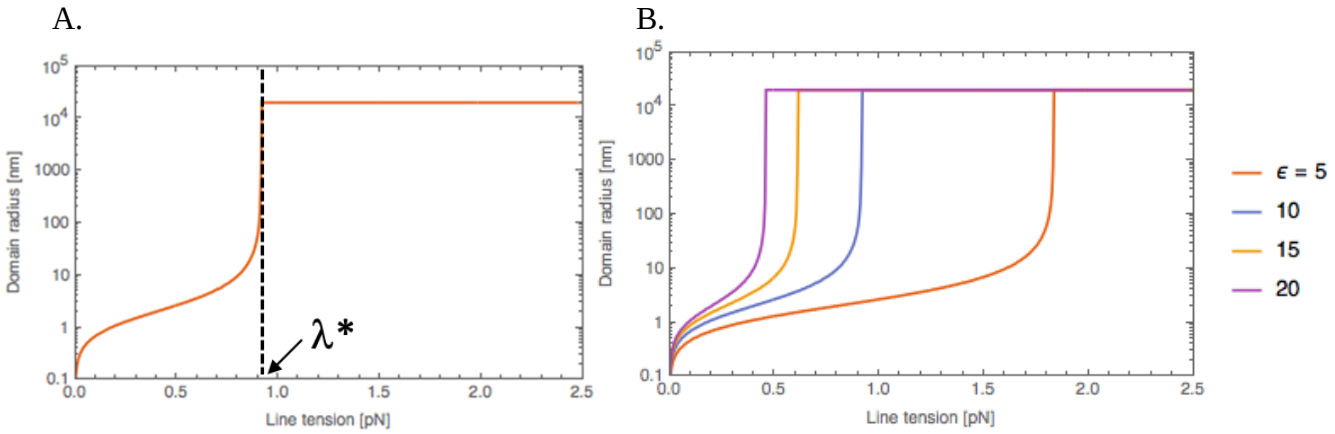

Fig. S16. Sensitivity of the continuum model to dielectric constant. (A) For a given parameter set, we define **λ*** as the line tension value where domain size reaches its limiting macroscopic value. (B) Increasing the dielectric constant over a reasonable range while holding other parameter values constant at their "canonical" values (Table S4) shifts the domain size transition to lower line tensions as the effects of electrostatics are diminished. In addition, we calculated **λ*** as a function of each individual parameter– ε, A_L, h and $\Delta\phi$ –while all other parameters were fixed, with the results shown in Fig. S17.

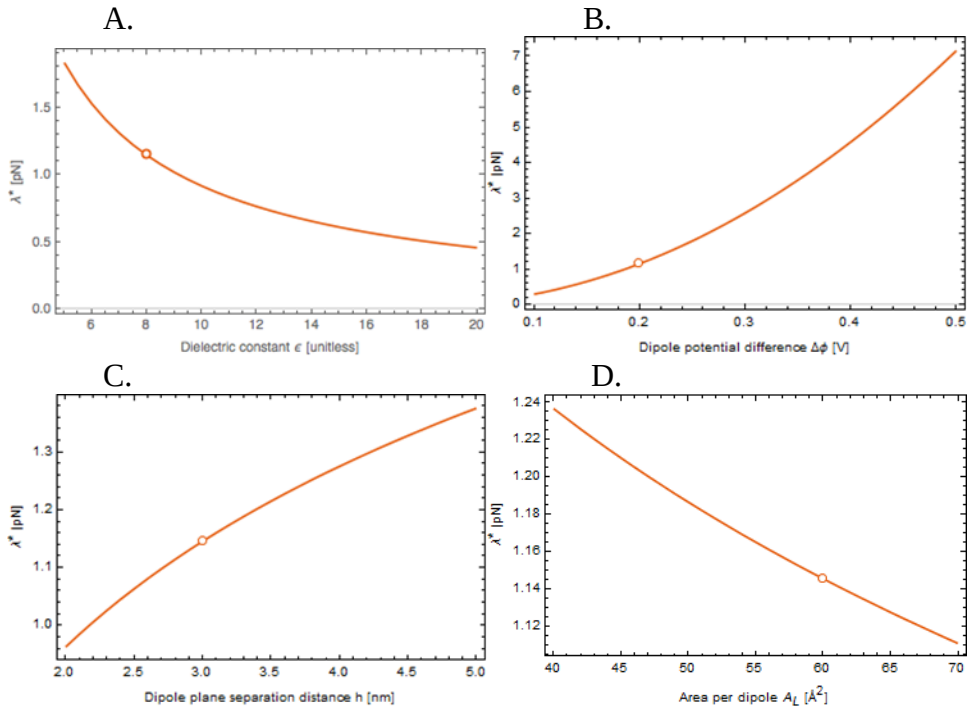

Fig. S17. Sensitivity of the continuum model to parameter values. (A) Varying the dielectric constant, ε, (at fixed dipole magnitude) over the range 5-20 results in critical line tension values from 0.45-1.8 pN (4-fold variation). (B) Varying the dipole potential difference, Δϕ, over the range 0.1-0.5 V results in critical line tension values from 0.2-7 pN (35-fold variation). (C) Varying the dipole plane separation distance, h, over the range 2-5 nm results in critical line tension values from 0.9-1.4 pN (1.5-fold variation). (D) Varying the area per dipole, A_L, over the range 40-70 Å^2 results in critical line tension values from 1.1-1.25 pN (1.1-fold variation). Open circle depicts **λ***, corresponding to the canonical parameters.

9. References

1. Angelova, M., S. Soleau, and P. Méléard. 1992. Preparation of giant vesicles by external AC electric fields. Kinetics and applications. Trends Colloid …. 89: 127–131.
2. Morales-Penningston, N.F., J. Wu, E.R. Farkas, S.L. Goh, T.M. Konyakhina, J.Y. Zheng, W.W. Webb, and G.W. Feigenson. 2010. GUV preparation and imaging: minimizing artifacts. Biochim. Biophys. Acta. 1798: 1324–32.
3. Esposito, C., A. Tian, S. Melamed, C. Johnson, S.-Y. Tee, and T. Baumgart. 2007. Flicker spectroscopy of thermal lipid bilayer domain boundary fluctuations. Biophys. J. 93: 3169–3181.
4. Heberle, F.A., R.S. Petruzielo, J. Pan, P. Drazba, N. Kučerka, R.F. Standaert, G.W. Feigenson, and J. Katsaras. 2013. Bilayer thickness mismatch controls domain size in model membranes. J. Am. Chem. Soc. 135: 6853–9.
5. Heberle, F.A., V.N.P. Anghel, and J. Katsaras. 2015. Scattering from phase-separated vesicles. I. An analytical form factor for multiple static domains. J. Appl. Crystallogr. 48: 1391–1404.
6. Feigin, L.A., and D.I. Svergun. 1987. Structure Analysis by Small-Angle X-Ray and Neutron Scattering. Boston, MA: Springer US.
7. Kučerka, N., J. Pencer, J.N. Sachs, J.F. Nagle, and J. Katsaras. 2007. Curvature Effect on the Structure of Phospholipid Bilayers. Langmuir. 23: 1292–1299.

8. Denbigh, K. 1981. The Principles of Chemical Equilibrium. Fourth. Cambridge University Press.
9. Heberle, F.A., J. Wu, S.L. Goh, R.S. Petruzielo, and G.W. Feigenson. 2010. Comparison of three ternary lipid bilayer mixtures: FRET and ESR reveal nanodomains. Biophys. J. 99: 3309–18.
10. Konyakhina, T.M., J. Wu, J.D. Mastroianni, F.A. Heberle, and G.W. Feigenson. 2013. Phase diagram of a 4-component lipid mixture: DSPC/DOPC/POPC/chol. Biochim. Biophys. Acta. 1828: 2204–14.
11. Petruzielo, R.S., F.A. Heberle, P. Drazba, J. Katsaras, and G.W. Feigenson. 2013. Phase behavior and domain size in sphingomyelin-containing lipid bilayers. Biochim. Biophys. Acta. 1828: 1302–13.
12. Zhao, J., J. Wu, F. a Heberle, T.T. Mills, P. Klawitter, G. Huang, G. Costanza, and G.W. Feigenson. 2007. Phase studies of model biomembranes: complex behavior of DSPC/DOPC/cholesterol. Biochim. Biophys. Acta. 1768: 2764–76.
13. Sodt, A.J., M.L. Sandar, K. Gawrisch, R.W. Pastor, and E. Lyman. 2014. The Molecular Structure of the Liquid-Ordered Phase of Lipid Bilayers. J. Am. Chem. Soc. 136: 725–732.
14. Ackerman, D.G., and G.W. Feigenson. 2015. Multiscale modeling of four-component lipid mixtures: Domain composition, size, alignment, and properties of the phase interface. J. Phys. Chem. B. 119.
15. Henriksen, J.R., and J.H. Ipsen. 2002. Thermal undulations of quasi-spherical vesicles stabilized by gravity. Eur. Phys. J. E. Soft Matter. 9: 365–74.
16. Gracià, R.S., N. Bezlyepkina, R.L. Knorr, R. Lipowsky, and R. Dimova. 2010. Effect of cholesterol on the rigidity of saturated and unsaturated membranes: fluctuation and electrodeformation analysis of giant vesicles. Soft Matter. 6: 1472.
17. Méléard, P., T. Pott, H. Bouvrais, and J.H. Ipsen. 2011. Advantages of statistical analysis of giant vesicle flickering for bending elasticity measurements. Eur. Phys. J. E. 34: 116.
18. Pécréaux, J., H.G. Döbereiner, J. Prost, J.F. Joanny, and P. Bassereau. 2004. Refined contour analysis of giant unilamellar vesicles. Eur. Phys. J. E. 13: 277–290.
19. Lakowicz, J.R. 2006. Principles of Fluorescence Spectroscopy Principles of Fluorescence Spectroscopy. .
20. Mills, T.T., G.E.S. Toombes, S. Tristram-Nagle, D.-M. Smilgies, G.W. Feigenson, and J.F. Nagle. 2008. Order parameters and areas in fluid-phase oriented lipid membranes using wide angle X-ray scattering. Biophys. J. 95: 669–81.
21. Alwarawrah, M., J. Dai, and J. Huang. 2010. A Molecular View of the Cholesterol Condensing Effect in DOPC Lipid Bilayers. J. Phys. Chem. B. 114: 7516–7523.
22. McConnell, H.M. 1991. Structures and Transitions in Lipid Monolayers at the Air-Water Interface. Annu. Rev. Phys. Chem. 42: 171–195.
23. http://stackoverflow.com/questions/28567166/uniformly-distribute-x-points-inside-a-circle